photonics

MDPI

Article

Energy-Gap Topology for Mapping Coupling Architectures in Lanthanide Co-Doped Photonic Materials

Helena Cristina Vasconcelos [1,2,*] and Maria Gabriela Meirelles [1,3]

[1] Faculty of Science and Technology, University of the Azores, 9500-321 Ponta Delgada, São Miguel, Azores, Portugal; maria.gf.meirelles@uac.pt
[2] Laboratory of Instrumentation, Biomedical Engineering and Radiation Physics (LIBPhys, UNL), Department of Physics, NOVA School of Science and Technology, NOVA University Lisbon, 2829-516 Caparica, Portugal
[3] Research Institute of Marine Sciences of the University of the Azores (OKEANOS), 9901-862 Horta, Faial, Azores, Portugal
* Correspondence: helena.cs.vasconcelos@uac.pt

Abstract

Lanthanide co-doped photonic materials are commonly interpreted through selected resonant transitions between assigned 4f multiplet states. Here, we introduce an energy-gap topology framework that compares Ln^{3+} ion pairs from the complete set of internal separations within their 4f manifolds. Reported multiplet-centre energies for a common LaF_3 spectroscopic reference were reduced to energy-only manifolds, from which normalized gap distributions were constructed. A symmetric descriptor, C_{A-B}, quantifies global similarity between complete gap distributions, whereas a directional descriptor, $D_{A\to B}$, measures the inclusion of the gaps of ion A within the occupied support of ion B. When applied to 11 trivalent lanthanide ions, this reveals distinct coupling architectures. Tb^{3+}–Ho^{3+}, Sm^{3+}–Dy^{3+}, Dy^{3+}–Ho^{3+}, Nd^{3+}–Ho^{3+}, and Er^{3+}–Ho^{3+} exhibit high symmetric overlap, defining a broad manifold–manifold topology signature. In contrast, Yb^{3+}-containing pairs show low global compatibility but high directional inclusion of the Yb^{3+} gap within the landscapes of candidate acceptor ions, such as Er^{3+}, Tm^{3+}, and Nd^{3+}, consistent with sparse-to-rich sensitizer-like architectures. The pairwise organization remains stable for bin widths between 250 and 1000 cm^{-1}. The descriptors provide a pre-spectroscopic screening map of energetic architecture; they do not predict the transfer efficiency, dominant mechanism, or final optical performance and should not be interpreted as host-independent constants.

Keywords: lanthanide photonics; rare-earth co-doping; energy-gap topology; 4f manifolds; manifold compatibility; directional gap matching; sensitizer–acceptor coupling; energy transfer; Yb^{3+} sensitization

Check for updates

Received: 17 June 2026
Revised: 27 July 2026
Accepted: 30 July 2026
Published: 31 July 2026

Copyright: © 2026 by the authors. Licensee MDPI, Basel, Switzerland. This article is an open access article distributed under the terms and conditions of the Creative Commons Attribution (CC BY) license.

1. Introduction

Lanthanide-doped photonic materials occupy a central position in optical spectroscopy, solid-state lighting, upconversion, near-infrared emission, optical thermometry, and energy-transfer-based photonic devices [1–3]. Their functionality arises from the partially shielded 4f electronic configuration of trivalent lanthanide ions, which gives rise to discrete multiplet manifolds, narrow optical transitions, and comparatively long-lived excited states [4–7]. These features make Ln^{3+} ions particularly attractive when well-defined electronic levels, radiative relaxation channels, and thermally coupled states are required [1–3,5,7].

The conventional interpretation of lanthanide photophysics is strongly transition-centred. Energy transfer, sensitization, cross-relaxation, and upconversion are usually discussed by identifying selected donor and acceptor levels whose energy separation is sufficiently close to permit resonant or quasi-resonant exchange [8–11]. This approach is physically well-founded and remains indispensable for detailed spectroscopic analysis, as actual optical behaviour depends on selection rules, oscillator strengths, multiphonon relaxation, site symmetry, concentration, ion–ion distances, and host-dependent phonon coupling [10,12–15]. However, a transition-centred description does not, by itself, provide a compact way to compare the overall energetic architecture of different lanthanide ion pairs.

This limitation becomes important in co-doped systems. Some lanthanide combinations are dominated by a small number of well-defined resonant channels. A typical case is a sensitizer–acceptor arrangement, where the sensitizer provides a restricted set of energetic separations that can feed selected excited states of a more complex acceptor ion [8–11]. Other combinations involve two ions with richer 4f manifolds, where several energy separations may be simultaneously available for relaxation, back-transfer, cross-relaxation, or redistribution among neighbouring levels [10,14–18]. In such cases, the relevant question is not just whether one transition matches another, but whether the two ions possess compatible landscapes of internal energy gaps.

Recent work on lanthanide-doped upconversion nanoparticles has further emphasized that energy transfer should be viewed not only as a set of isolated resonant events but as a designable network of coupled pathways as well. Concepts such as energy-transfer editing, energy-transfer designing, collective energy-transfer networks, Yb^{3+}-mediated migration, topologically organized dopant architectures, and size-dependent energy-transfer amplification have shown that the optical response of rare-earth-doped materials can depend strongly on how energetic pathways are organized across the dopant system [2,3,16–21]. These developments motivate descriptors that can compare ion-pair architectures before detailed material-specific modelling is undertaken. In the present work, the term topology is used operationally to describe the organization, overlap, and directional inclusion of internal energy-gap distributions. It does not denote a topological invariant in the strict mathematical sense and is distinct from the spatial topology of dopants, sublattices, or core–shell structures.

Accordingly, the term energy-gap topology is used here as a compact description of the mapped organization of populated gap regions, gap-distribution overlap, support coverage, and directional inclusion. It should be read as an operational topology map of energetic architecture and not as a formal mathematical invariant, nor as a description of the spatial arrangement of dopant ions.

This distinction motivates a change in viewpoint. Instead of starting from assigned transitions, one may ask what energetic information is contained in the complete set of multiplet-centre energies of a given Ln^{3+} ion. If the spectroscopic identity of each level is temporarily suppressed, each ion can be represented by an energy-only manifold as

$$M_{\mathrm{Ln}} = \{E_i\}.$$

From this manifold, all internal energetic separations can be constructed as

$$\Delta E_{ij} = \mid E_i - E_j \mid .$$

The resulting set of gaps defines a distribution,

$$P_{\mathrm{Ln}}(\Delta E),$$

which describes the energetic separations made available by the 4f manifold as a whole. This representation does not replace the spectroscopic assignment of individual levels. Instead, it provides a complementary view of the energy architecture on which transition-specific mechanisms are built.

A single scalar descriptor is not sufficient to describe all relevant co-doping situations. If two ions have similar gap distributions, they may support broad manifold–manifold compatibility, because many energetic separations are available in both systems. This requires a symmetric descriptor, denoted here as C_{A-B}, which measures the global similarity between the gap distributions of ions A and B. However, sensitizer–acceptor systems can be highly asymmetric. A sparse sensitizer manifold may contain only one or a few relevant gaps, but those gaps may still match separations within a much richer acceptor manifold. Such cases require a directional descriptor, denoted here as $D_{A\to B}$, which measures how well the gaps of ion A are represented within the gap landscape of ion B.

The combined use of C_{A-B} and $D_{A\to B}$ separates two physically different coupling architectures. High C_{A-B}, together with high directional matching in both directions, identifies ion pairs whose manifolds are broadly compatible and may support manifold-mediated energetic redistribution. In contrast, low C_{A-B} combined with high $D_{A\to B}$ in one direction identifies directional sensitizer-like systems, where a limited set of donor gaps can match selected acceptor separations without requiring global similarity between the two manifolds. This distinction is essential, as a low global manifold compatibility does not necessarily imply poor photophysical relevance; it may instead indicate that the pair operates through a restricted directional channel.

This approach is useful for researchers working with Ln^{3+} co-doped materials because it provides a pre-spectroscopic map of ion-pair energetic architectures. Before detailed lifetime measurements, Judd–Ofelt analysis, rate-equation modelling, or host-specific optimization are performed, the topology of the energy gaps can indicate whether a candidate pair should be approached as a broad manifold–manifold system or as a directional sensitizer–acceptor system [8–15]. The method therefore does not aim to rank lanthanide pairs by expected emission intensity or device performance. Its purpose is to identify the type of energy-transfer physics that is more naturally suggested by the energetic architecture of the ions involved.

Because this representation is deliberately energy-only, it does not include oscillator strengths, transition probabilities, selection rules, spectral overlap integrals, phonon-assisted mismatch, local site symmetry, dopant concentration, or donor–acceptor distance. These factors determine the actual transfer rates, branching ratios, and emission efficiency in real materials. The descriptors introduced here therefore identify energetic compatibility patterns to be tested experimentally; they do not constitute evidence for an experimentally realized energy-transfer mechanism.

In this work, the reported Ln^{3+} multiplet-centre energies for a common LaF_3 spectroscopic reference, using observed centres where available and calculated centres from fitted spectroscopic models otherwise, are reorganized into energy-only manifolds and used to construct gap distributions across a series of trivalent lanthanide ions [7,22]. A symmetric compatibility descriptor, C_{A-B}, and a directional matching descriptor, $D_{A\to B}$, are then calculated for all ion pairs. The novelty of this approach lies in replacing conventional transition-by-transition matching with a whole-manifold representation and in separating two forms of energetic matching that are not equivalent: global manifold compatibility and directional gap inclusion. The combined descriptors show that broad manifold–manifold pairs and sparse sensitizer–acceptor pairs cannot be placed on a single compatibility scale because they correspond to distinct energetic coupling architectures. The resulting topology map reveals pairs with strong manifold-level compatibility, such as Tb^{3+}–Ho^{3+}, Sm^{3+}–Dy^{3+},

Dy^{3+}–Ho^{3+}, Nd^{3+}–Ho^{3+}, and Er^{3+}–Ho^{3+}, as well as Yb^{3+}-containing combinations that are better described as directional sensitizer-like systems. The proposed framework therefore introduces a pre-spectroscopic mapping layer that precedes transition-specific, host-dependent kinetic modelling. The conceptual workflow of the approach is summarized in Figure 1.

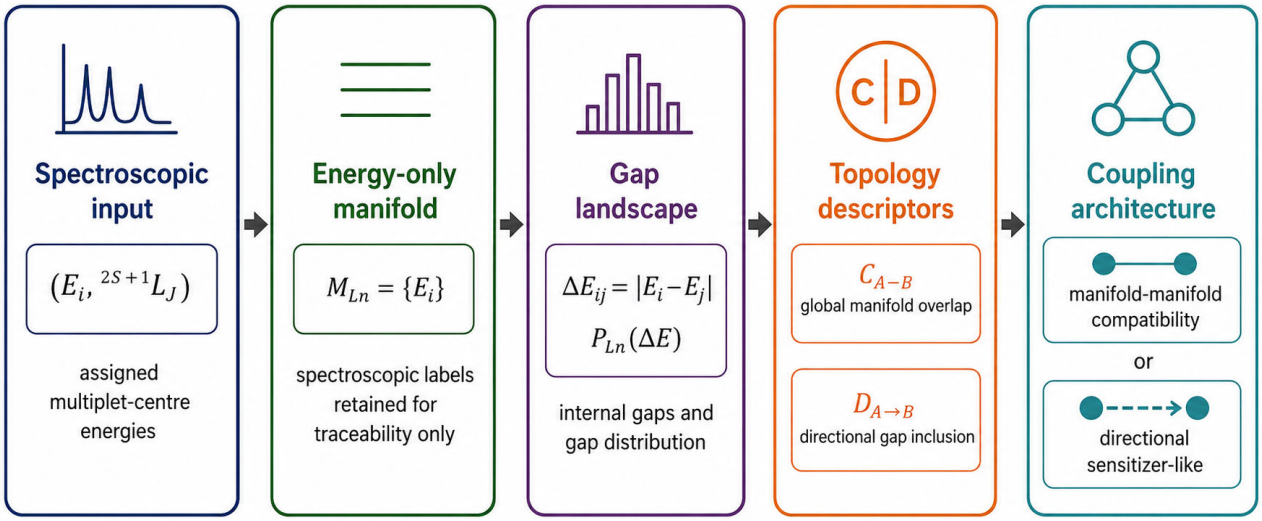


Figure 1. Energy-gap topology workflow for mapping Ln^{3+}–Ln^{3+} coupling architectures. Assigned multiplet-centre energies are reduced to energy-only manifolds, from which internal gaps and gap distributions are constructed. The complementary descriptors C_{A-B} and $D_{A\to B}$ are then used to distinguish broad manifold–manifold compatibility from directional sensitizer-like coupling.

2. Materials and Methods

2.1. Energy-Level Data

The analysis was based on the multiplet-centre energies reported for trivalent lanthanide ions in LaF_3, using observed centres where available and calculated centres from the fitted spectroscopic models otherwise [7,22]. For each ion, the tabulated spectroscopic information contains the energy of each multiplet centre together with its conventional term assignment [7,22]. The term labels were retained for data traceability but were not used in the numerical descriptors calculated in this work.

The lanthanide series considered here included Ce^{3+}, Pr^{3+}, Nd^{3+}, Sm^{3+}, Gd^{3+}, Tb^{3+}, Dy^{3+}, Ho^{3+}, Er^{3+}, Tm^{3+}, and Yb^{3+}. These ions provide a broad range of 4f configurations, from sparse manifolds, such as Ce^{3+} and Yb^{3+}, to richer multiplet structures, such as Tb^{3+} and Ho^{3+}. All energies were treated in cm^{-1} [7,22]. All ions were compared using multiplet-centre energies reported for the same LaF_3 spectroscopic reference. This common-host basis minimizes inconsistencies that would arise from combining level schemes obtained in different materials. Nevertheless, the resulting descriptor values are specific to this reference dataset and should not be interpreted as universal host-independent constants. Crystal-field shifts, Stark splitting, local symmetry, and host-phonon energy may modify the detailed energetic matching in a particular material.

For each ion, the input table was organized using the following fields:

$$\text{ion}, n_f, E_i, \text{ term label}, J, \text{ source}, \text{ table/figure}, \text{ page}, \text{ data type}, \text{ and notes}.$$

Only the ion identity and the energy coordinate E_i entered the topology calculations; n_f was retained for ordering and annotation. The remaining columns were kept as audit fields to ensure source traceability.

2.2. Construction of Energy-Only Manifolds

For each lanthanide ion, the assigned spectroscopic representation is given as

$$\left(E_i, {}^{2S+1}L_J, J\right)$$

which is then reduced to an energy-only manifold

$$M_{\mathrm{Ln}} = \{E_1, E_2, \ldots, E_N\}, \tag{1}$$

where N is the number of multiplet-centre energies available for that ion.

This reduction does not imply that term labels or angular momentum assignments are physically irrelevant. Instead, it defines a deliberately label-free representation in which the comparison between ions is based only on the energetic architecture of their 4f manifolds.

2.3. Pairwise Internal Energy Gaps

For each ion, all pairwise internal energy separations were calculated as

$$\Delta E_{ij} = \mid E_i - E_j \mid, i < j. \tag{2}$$

The complete set of non-zero separations defines the gap set of ion Ln as

$$G_{\mathrm{Ln}} = \{\Delta E_{ij}\}. \tag{3}$$

Zero-energy separations, when produced by repeated or coincident reported energies, were excluded from the gap distributions because they do not represent finite energetic exchange channels. The multiplicity of non-zero gaps was retained, since repeated or closely spaced separations contribute to the density of available energetic pathways. Multiplicity is treated here as a structural weight within the gap landscape and not as a spectroscopic transition probability. Accordingly, the gap set represents an internal energetic architecture rather than a list of optically allowed or thermally accessible transitions.

For an ion with N levels, the maximum number of pairwise gaps is

$$N_{\mathrm{gap}} = \frac{N(N-1)}{2}. \tag{4}$$

Sparse manifolds, such as Ce^{3+} and Yb^{3+}, therefore generate only one non-zero gap, whereas ions with richer multiplet structures generate much denser gap landscapes.

2.4. Gap Distributions

The gap set of each ion was converted into a normalized distribution, $P_{\mathrm{Ln}}(\Delta E)$, using a common energy grid for all ions. A bin width of 500 cm^{-1} was used throughout the analysis. For each tested bin width, the common grid started at 0 cm^{-1}, used identical bin edges for all ions, and extended beyond the largest gap in the complete dataset.

The 500 cm^{-1} bin width was used for the primary analysis because it provides a compromise between energetic resolution and statistical occupancy for ions with markedly different numbers of internal gaps. To test whether the conclusions depended on this discretization choice, the complete calculation was repeated using bin widths of 250, 750, and 1000 cm^{-1}. Descriptor values, pairwise rankings, and the relative positions of representative manifold–manifold and directional sensitizer-like pairs were compared across the four binning conditions.

The 500 cm^{-1} value should therefore be regarded as a numerical resolution used to compare multiplet-centre gap distributions and not as a universal physical linewidth.

Narrower bins increase the energetic resolution but can generate sparse occupancy for ions with few internal gaps, whereas broader bins improve occupancy at the cost of merging nearby gap regions. Alternative statistical comparisons, including kernel-density estimates, Jensen–Shannon divergence, earth mover's distance, or graph-based descriptors, may be useful in future extensions, particularly when denser, host-specific, Stark-level datasets are available.

For each bin k, the normalized gap density was calculated as

$$P_{\mathrm{Ln}}(k) = \frac{n_{\mathrm{Ln}}(k)}{\sum_k n_{\mathrm{Ln}}(k)}, \tag{5}$$

where $n_{\mathrm{Ln}}(k)$ is the number of non-zero gaps of ion Ln falling within bin k, thus giving

$$\sum_k P_{\mathrm{Ln}}(k) = 1.$$

Using a common binning scheme ensured that all lanthanide ions were compared on the same energetic scale. The resulting distribution describes how the internal energy separations of each ion are distributed across the 4f manifold. For Figure 2 only, continuous profiles were generated from the binned distributions using the same visualization procedure for all ions. These profiles were not used in the calculation of any topology descriptor.

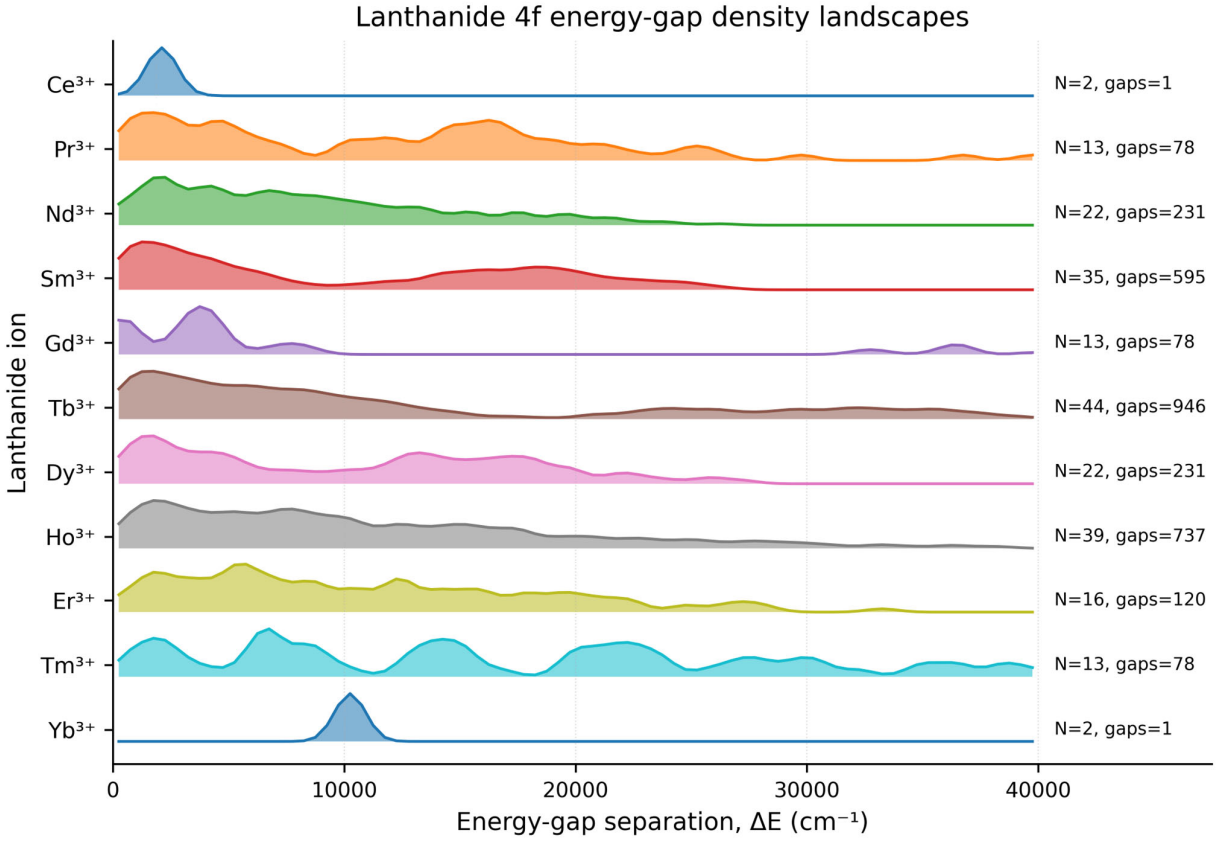


Figure 2. Ridgeline visualization of the normalized energy-gap distributions for the Ln^{3+} ions considered in this work. Each profile was constructed from non-zero internal gaps generated from the corresponding energy-only manifold. The values to the right indicate the number of multiplet-centre energies, N, and the number of non-zero pairwise gaps used for each ion. Continuous profiles are used exclusively as visual guides for the underlying binned distributions; all numerical descriptors were calculated from unsmoothed normalized histograms.

2.5. Symmetric Manifold-Compatibility Descriptor

To quantify the global similarity between two gap distributions, the symmetric compatibility descriptor was calculated using:

$$C_{A-B} = \frac{\sum_k P_A(k) P_B(k)}{\left[\left(\sum_k P_A(k)^2\right)\left(\sum_k P_B(k)^2\right)\right]^{1/2}}. \quad (6)$$

This descriptor is equivalent to a normalized overlap between the two gap-density vectors, satisfying

$$0 \leq C_{A-B} \leq 1$$

and

$$C_{A-B} = C_{B-A}.$$

High C_{A-B} indicates that two ions have similar gap-density landscapes and therefore broad manifold-level energetic compatibility. Low C_{A-B} indicates that the two manifolds do not have globally similar gap distributions.

However, C_{A-B} alone cannot distinguish all physically relevant co-doping situations. In particular, sensitizer–acceptor systems may be strongly directional: a sparse donor ion may have only one or a few gaps, but those gaps may still match selected separations in a richer acceptor manifold [8–11]. For this reason, a second descriptor was introduced.

2.6. Directional Gap-Matching Descriptor

To quantify directional gap inclusion, a descriptor $D_{A\to B}$ was defined. For each ion B, a binary support function was constructed:

$$S_B(k) = \begin{cases} 1, & P_B(k) > 0, \\ 0, & P_B(k) = 0. \end{cases} \quad (7)$$

The directional matching from ion A to ion B was then calculated as

$$D_{A\to B} = \sum_k P_A(k) S_B(k). \quad (8)$$

Thus, $D_{A\to B}$ measures the fraction of the gap distribution of ion A that falls within energy regions also occupied by gaps of ion B, satisfying

$$0 \leq D_{A\to B} \leq 1.$$

Unlike C_{A-B}, this descriptor is directional:

$$D_{A\to B} \neq D_{B\to A}.$$

An important consequence of this definition is that $D_{A\to B} = 1$ does not have the same informational content for sparse and dense manifolds. For an ion A containing a single non-zero internal gap, such as Yb^{3+}, $D_{A\to B} = 1$ indicates only that this single gap falls within an energy bin occupied by ion B. It does not demonstrate that the corresponding energetic match is unique, statistically exceptional, or experimentally efficient, nor does it constitute direct evidence of energy transfer.

To contextualize directional inclusion, the fractional support coverage of ion B was calculated within the active energy domain of each ordered pair $A \to B$. The pairwise energy domain was defined as

$$\Omega_{A,B} = \left[0, E_{A,B}^{\max}\right], E_{A,B}^{\max} = \max(\max G_A, \max G_B). \quad (9)$$

The fractional support coverage was then calculated as

$$F_B^{(A,B)} = \frac{N_{\mathrm{occ},B}^{(A,B)}}{N_\Omega^{(A,B)}}, \tag{10}$$

where $N_{\mathrm{occ},B}^{(A,B)}$ is the number of bins occupied by ion B within $\Omega_{A,B}$, and $N_\Omega^{(A,B)}$ is the total number of bins in the same pairwise domain.

A high value of $F_B^{(A,B)}$ indicates that ion B occupies a broad fraction of the energy domain relevant to the pair, whereas a low value indicates a more restricted support. Consequently, complete directional inclusion within a relatively narrow acceptor support is more selective than complete inclusion within a broadly occupied support.

The directional descriptor was therefore interpreted jointly with C_{A-B}, the reverse matching value $D_{B\to A}$, the directional asymmetry defined in Equation (12), and the pair-dependent support coverage $F_B^{(A,B)}$.

None of these quantities was interpreted individually as a measure of energy-transfer probability or efficiency.

For one-gap ions, the directional descriptor is therefore best viewed as a support-inclusion test rather than as a weighted measure of transfer propensity. Future implementations could introduce additional physical weights—for example, oscillator strength, transition probability, phonon-assisted energy mismatch, spectral-overlap weighting, or concentration-dependent interaction terms—provided that such quantities are available for the host and transitions under study.

This directionality remains physically informative. If $D_{A\to B}$ is high but $D_{B\to A}$ is low, the gaps of ion A are largely represented within the occupied support of ion B, whereas the richer gap landscape of B is not reciprocally represented within A. This pattern is topologically consistent with a sparse-to-rich sensitizer-like architecture, in which a donor or sensitizer may match selected acceptor separations without requiring broad manifold–manifold similarity [8–11]. The descriptor identifies the energetic architecture suggested by the gap distributions; confirmation of an actual donor–acceptor mechanism requires material-specific spectroscopic and kinetic measurements.

2.7. Interpretation of Coupling Architectures

The descriptors C_{A-B}, $D_{A\to B}$, and $D_{B\to A}$ were interpreted together to characterize energetic coupling architectures.

Pairs with high C_{A-B} and high directional matching in both directions were interpreted as candidate manifold–manifold architectures. In these cases, the two ions possess broadly overlapping gap landscapes, suggesting that several energetic separations may participate in relaxation, redistribution, cross-relaxation, or back-transfer processes [10,14,15].

Pairs with low C_{A-B}, high $D_{A\to B}$ in one direction, and low $D_{B\to A}$ in the reverse direction were interpreted as candidate directional sensitizer-like architectures. In these cases, the manifolds are not globally similar, but the gaps of one ion are contained within selected regions of another ion's gap landscape. This topology pattern is consistent with systems in which a sparse sensitizer may feed a richer acceptor through a restricted number of resonant or quasi-resonant channels [8–11].

Pairs with low C_{A-B} and low directional matching in both directions were interpreted as having a weak topology match under the present gap-distribution criterion.

For compact visualization, two derived quantities were also considered:

$$D_{\mathrm{bi}} = \min(D_{A\to B}, \quad D_{B\to A}), \tag{11}$$

which measures bidirectional gap inclusion, and

$$A_D = | D_{A\to B} - D_{B\to A} |, \tag{12}$$

which measures directional asymmetry. High D_{bi} indicates reciprocal manifold inclusion, whereas high A_D indicates strongly asymmetric matching.

The terms manifold–manifold, directional sensitizer-like, intermediate/mixed, and weak topology match were used as relative interpretive labels within the pairwise landscape obtained from the same dataset. They do not define universal numerical thresholds or mechanistic assignments. The regions shown in the coupling-architecture map indicate characteristic combinations of C_{A-B} and directional asymmetry, whereas individual pair interpretation also considers $D_{A\to B}$, $D_{B\to A}$, acceptor support coverage, and stability under changes in bin width. The map should therefore be read as a screening representation of energetic architecture rather than as a deterministic classifier of experimental energy-transfer mechanisms.

For the coupling-architecture map presented in Section 3.5, the descriptive visual regions were assigned as follows: manifold–manifold, $C_{A-B} \geq 0.80$ and $A_D \leq 0.25$; directional sensitizer-like, $C_{A-B} \leq 0.30$ and $A_D \geq 0.90$; weak topology match, $C_{A-B} \leq 0.30$ and $A_D \leq 0.30$; and intermediate/mixed for all remaining pairs. These boundaries were used exclusively to organize the visual map and are not proposed as universal physical thresholds.

Thus, the qualitative concepts of reciprocal manifold compatibility and directional sparse-to-rich inclusion are intended to be transferable, whereas the numerical boundaries used to label the regions are dataset-dependent. If the method is applied to another host, to Stark-resolved-level schemes, or to a differently weighted descriptor, the boundaries should be recalibrated from the resulting pairwise landscape.

2.8. Computational Workflow and Quality Control

All calculations were performed from the verified energy-level tables using a reproducible workflow:

$$\begin{aligned}\text{source energy table} \to \text{energy-only manifold} \to \text{pairwise gaps} \to \text{gap distribution}\\ \to C_{A-B} \text{ and } D_{A\to B} \to \text{coupling-architecture map.}\end{aligned}$$

Quality control included checking the number of levels per ion, the number of generated pairwise gaps, the exclusion of zero gaps from the distributions, the use of a common energy grid for all ions, and the recomputation of pairwise descriptors from the final verified tables [7,22]. Spectroscopic labels, emission wavelengths, oscillator strengths, transition probabilities, lifetimes, and prior knowledge of known co-doped systems were not used in the calculation of C_{A-B} or $D_{A\to B}$.

The descriptors therefore quantify energetic architectures only. They are intended to characterize the type of coupling suggested by the gap topology of an ion pair before host-specific optical modelling or material-specific experimental optimization is undertaken.

The supplied reproducibility script was tested under Python 3.13.5 with NumPy 2.3.5, and figure preparation used Matplotlib 3.10.8. The script recomputes the energy-gap distributions, pairwise topology descriptors, bin-width sensitivity analysis, and pair-dependent support-coverage controls and is provided in the Supplementary Materials.

2.9. Sensitivity and Support-Coverage Controls

Two complementary robustness controls were applied. First, the complete gap-distribution analysis was repeated using bin widths of 250, 500, 750, and 1000 cm^{-1}. For

each bin width, all $P_{\mathrm{Ln}}(\Delta E)$, C_{A-B}, $D_{A\to B}$, $D_{B\to A}$, D_{bi}, and directional-asymmetry values were recalculated directly from the verified energy-level tables. Robustness was assessed from the rank correlation of the complete pairwise landscapes and from the behaviour of representative pairs.

Second, the pair-dependent fractional support coverage $F_B^{(A,B)}$ was calculated within the active energy domain of each ordered pair. This control is particularly relevant for sparse ions, such as Ce^{3+} and Yb^{3+}, for which a directional value of unity can result from a single gap falling within an occupied acceptor bin. The support-coverage analysis distinguishes complete directional inclusion from the breadth of the acceptor support in which that inclusion occurs. The directional descriptor was therefore not interpreted in isolation or as a statistical probability of energy transfer.

3. Results and Discussion

3.1. Energy-Gap Landscapes of Individual Ln^{3+} Manifolds

The first outcome of the analysis is the transformation of each Ln^{3+} energy-level scheme into a gap-density landscape. Starting from the reported multiplet-centre energies for Ln^{3+} ions in LaF_3 [7,22], each ion was represented by an energy-only manifold, $M_{\mathrm{Ln}} = \{E_i\}$, and all non-zero internal separations were calculated. This operation converts a conventional spectroscopic level scheme, normally described in terms of assigned 4f multiplet states [4–7], into a distribution of available energetic separations as $P_{\mathrm{Ln}}(\Delta E)$. Figure 2 shows the resulting gap-density landscapes for the Ln^{3+} ions considered in this work.

The resulting gap landscapes differ strongly across the lanthanide series. Ions with sparse 4f manifolds, such as Ce^{3+} and Yb^{3+}, generate only one non-zero internal gap. In contrast, ions with richer manifolds generate far denser sets of possible separations. For example, Er^{3+} generates 120 pairwise gaps, whereas Ho^{3+} has 39 multiplet-centre energies, corresponding to 741 possible pairwise separations, of which 737 are non-zero after removal of coincident reported energies. Tb^{3+} and Sm^{3+} also produce dense gap landscapes, with several hundred available internal separations.

This difference is important because the number of levels alone does not determine the topology of the energetic landscape. Two ions may have a comparable number of levels but different distributions of separations, depending on how their multiplet energies are arranged. Conversely, ions with different numbers of levels may still share similar gap-density regions if their internal separations are distributed over comparable energy intervals. Therefore, the gap distribution $P_{\mathrm{Ln}}(\Delta E)$ provides a more informative representation than a simple count of energy levels.

The distributions reveal that the rare-earth ions do not simply differ by the number of their available levels but also by the way their internal separations populate the energy scale. This provides the basis for comparing ion pairs in terms of their energetic architecture rather than the selected labelled transitions.

3.2. Symmetric Manifold Compatibility from C_{A-B}

The symmetric descriptor C_{A-B} was first used to quantify the global similarity between the gap distributions of all ion pairs. Since $C_{A-B} = C_{B-A}$, this descriptor measures reciprocal manifold-level compatibility rather than a donor–acceptor direction. High values indicate that two ions possess broadly similar distributions of internal energy separations.

The highest values of C_{A-B} were obtained for pairs involving relatively rich manifolds. Representative high-compatibility pairs include Tb^{3+}–Ho^{3+}, Sm^{3+}–Dy^{3+}, Dy^{3+}–Ho^{3+}, Nd^{3+}–Ho^{3+}, Nd^{3+}–Tb^{3+}, and Er^{3+}–Ho^{3+}. These pairs do not simply correspond to neighbouring ions in the lanthanide series. Instead, they correspond to pairs whose gap-density landscapes overlap strongly over the energy scale used in the analysis.

A representative ranking of high-C pairs is shown in Table 1.

Table 1. Representative ion pairs with high symmetric manifold compatibility.

Pair	C_{A-B}	Interpretation
Tb^{3+}–Ho^{3+}	0.908	strong manifold–manifold compatibility
Sm^{3+}–Dy^{3+}	0.870	strong manifold–manifold compatibility
Dy^{3+}–Ho^{3+}	0.859	strong manifold–manifold compatibility
Nd^{3+}–Ho^{3+}	0.859	strong manifold–manifold compatibility
Nd^{3+}–Tb^{3+}	0.846	strong manifold–manifold compatibility
Er^{3+}–Ho^{3+}	0.845	strong manifold–manifold compatibility
Pr^{3+}–Sm^{3+}	0.843	strong manifold–manifold compatibility
Sm^{3+}–Ho^{3+}	0.838	strong manifold–manifold compatibility

The physical meaning of high C_{A-B} is not that a given pair will necessarily display high emission intensity or high energy-transfer efficiency. Rather, high C_{A-B} indicates that the two ions possess similar gap architectures. Such pairs are expected to be more naturally described as manifold–manifold systems, where several energetic separations may be simultaneously available for relaxation, cross-relaxation, back-transfer, or population redistribution [2,3,10,16].

This interpretation is particularly relevant for pairs such as Er^{3+}–Ho^{3+}. The value $C_{Er-Ho} = 0.845$ places this pair within the high-compatibility region of the lanthanide-pair landscape. The result does not identify a single $Er^{3+} \rightarrow Ho^{3+}$ or $Ho^{3+} \rightarrow Er^{3+}$ transition. Instead, it indicates that the two ions share a broad set of compatible internal separations, consistent with a manifold-mediated coupling architecture.

3.3. Why Symmetric Compatibility Alone Is Insufficient

Although C_{A-B} captures global manifold similarity, it cannot describe all physically relevant co-doping architectures. This limitation becomes clear for Yb^{3+}-containing systems.

Yb^{3+} has a sparse 4f manifold and therefore generates only one non-zero internal gap [7,22]. As a result, its complete gap distribution cannot resemble the much richer gap distributions of ions, such as Er^{3+}, Tm^{3+}, or Nd^{3+}. Consequently, the symmetric compatibility values for Yb^{3+}-containing pairs are low; for example,

$$C_{Er-Yb} = 0.145,$$

$$C_{Tm-Yb} = 0.082,$$

and

$$C_{Nd-Yb} = 0.118.$$

Because Yb^{3+} generates only one non-zero internal gap, the directional descriptor requires a specific interpretation in this case. $D_{Yb \rightarrow B} = 1$ means that the Yb^{3+} gap is included within the occupied support of ion B; it does not imply that the corresponding resonance is unique, statistically exceptional or experimentally efficient. The physical relevance of a Yb^{3+}-containing pair must therefore be assessed from the combined pattern of low global compatibility, high forward inclusion, low reverse inclusion, and strong directional asymmetry.

If C_{A-B} were the only descriptor, these pairs would appear weakly compatible at the manifold level. However, such an interpretation would be incomplete, because Yb^{3+}-containing pairs are known to operate through strongly directional sensitizer–acceptor mechanisms [10,11,17,18]. The relevant question is not whether the full Yb^{3+} gap distribu-

tion resembles the full Er^{3+}, Tm^{3+}, or Nd^{3+} distribution. Instead, the relevant question is whether the sparse Yb^{3+} gap is represented within the gap landscape of the acceptor ion.

This motivates the directional descriptor $D_{A\to B}$. While C_{A-B} asks whether two complete gap distributions are globally similar, $D_{A\to B}$ asks whether the gaps of ion A are contained within the gap landscape of ion B. This distinction is the key to separating manifold–manifold compatibility from sensitizer-like directional matching.

3.4. Directional Gap Matching and Sensitizer-like Architectures

This directional pattern is particularly clear for Yb^{3+}-containing systems. These pairs show low global manifold compatibility because Yb^{3+} has a sparse 4f manifold and therefore cannot reproduce the dense gap distributions of ions, such as Er^{3+}, Tm^{3+}, or Nd^{3+} [7,22]. However, the directional descriptor shows that the Yb^{3+} gap is represented within the gap landscapes of selected acceptor ions. The contrast between symmetric compatibility and directional asymmetry is summarized in Figure 3, and representative examples are given in Table 2.

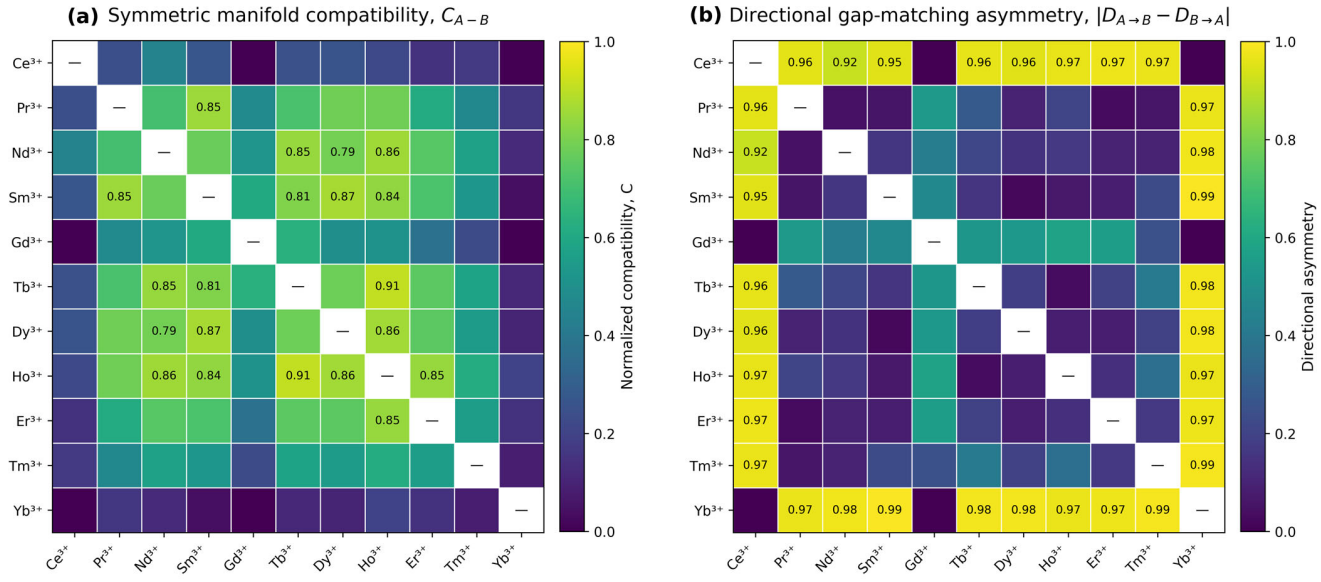


Figure 3. Pairwise Ln^{3+}–Ln^{3+} descriptor matrices. (**a**) Symmetric manifold-compatibility matrix C_{A-B}, measuring global overlap between normalized gap distributions. (**b**) Directional gap-matching asymmetry matrix $|\ D_{A\to B} - D_{B\to A}\ |$, highlighting pairs for which gap inclusion is strongly directional.

Table 2. Representative comparison between symmetric compatibility and directional gap matching.

Pair	C_{A-B}	$D_{A\to B}$	$D_{B\to A}$	Coupling Architecture
Er^{3+}–Ho^{3+}	0.845	$D_{Er\to Ho} = 1.000$	$D_{Ho\to Er} = 0.860$	manifold–manifold
Yb^{3+}–Er^{3+}	0.145	$D_{Yb\to Er} = 1.000$	$D_{Er\to Yb} = 0.025$	directional sensitizer-like
Yb^{3+}–Tm^{3+}	0.082	$D_{Yb\to Tm} = 1.000$	$D_{Tm\to Yb} = 0.013$	directional sensitizer-like
Yb^{3+}–Nd^{3+}	0.118	$D_{Yb\to Nd} = 1.000$	$D_{Nd\to Yb} = 0.022$	directional sensitizer-like

These results show that low C_{A-B} does not necessarily indicate that a pair is physically irrelevant. Instead, low C_{A-B} combined with high $D_{A\to B}$ in one direction identifies a different type of energetic architecture. In Yb^{3+}-containing systems, the sparse Yb^{3+} gap can be included within the richer gap landscape of an acceptor ion, even though the two complete manifolds are not globally similar.

The identical value $D_{Yb\to B} = 1$ for the three Yb^{3+}-containing examples does not imply identical energetic selectivity. At the primary bin width of 500 cm^{-1}, the fractional support

coverages of the acceptor manifolds within the corresponding pairwise energy domains were $F_{\mathrm{Er}}^{(\mathrm{Yb,Er})} = 0.716$, $F_{\mathrm{Tm}}^{(\mathrm{Yb,Tm})} = 0.358$, and $F_{\mathrm{Nd}}^{(\mathrm{Yb,Nd})} = 0.811$. Thus, the Yb^{3+} gap is included in all three acceptor supports, but this inclusion occurs within a substantially narrower fractional support for Tm^{3+} than for Er^{3+} or Nd^{3+}. These values reinforce the need to interpret $D_{A\to B}$ together with support coverage and reverse directional matching rather than as an isolated measure of transfer propensity.

This topology pattern is consistent with a sensitizer-like architecture. A simple donor or sensitizer does not need to reproduce the full energetic structure of the acceptor. It only needs to provide one or a few separations that can feed selected acceptor levels [2,3,10,11,17,18]. The directional descriptor captures this situation because it is sensitive to gap inclusion rather than to full-distribution similarity.

In contrast, the Er^{3+}–Ho^{3+} pair shows high symmetric compatibility and high directional matching in both directions. This indicates a different energetic architecture. The Er^{3+}–Ho^{3+} pair is not topologically represented as a sparse sensitizer feeding a richer acceptor through a single restricted channel. Instead, their manifolds share a broad set of compatible internal separations, consistent with a manifold–manifold coupling regime.

3.5. Coupling-Architecture Map

The combined use of C_{A-B}, $D_{A\to B}$, and $D_{B\to A}$ allows each ion pair to be placed in a coupling-architecture map. This map provides a descriptive separation of four characteristic regions within the present dataset. Figure 4 shows the resulting topology-based map of the Ln^{3+}–Ln^{3+} pairs considered in this work.

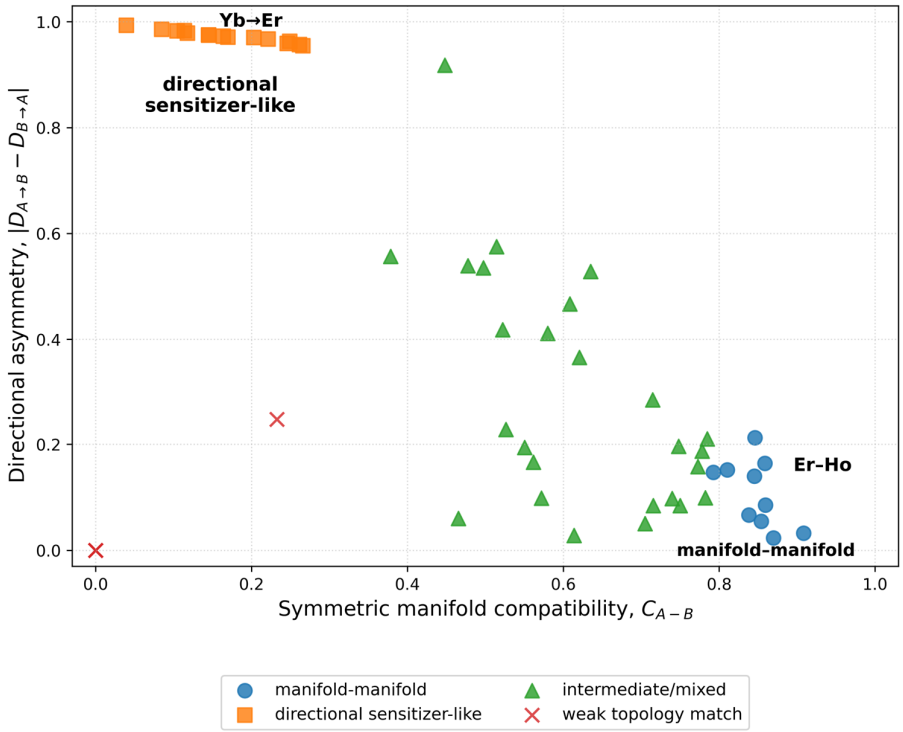


Figure 4. Coupling-architecture map obtained by combining symmetric manifold compatibility with directional gap-matching asymmetry. High-C_{A-B}, low-asymmetry pairs define the manifold–manifold region, whereas low-C_{A-B}, high-asymmetry pairs define directional sensitizer-like architectures. Pairs located between these limiting regions are shown as intermediate/mixed, whereas low-compatibility pairs without strong directional inclusion are shown as weak topology matches. Er^{3+}–Ho^{3+} and $Yb^{3+} \to Er^{3+}$ are shown as representative examples of the two limiting regimes. The labelled regions are interpretive guides within the present LaF_3-based dataset and do not represent universal decision boundaries or direct assignments of experimental transfer mechanisms.

The first region corresponds to high C_{A-B} and high bidirectional matching. These pairs possess similar gap-density landscapes and reciprocal gap inclusion. This region is interpreted as a candidate manifold–manifold architecture—examples include Tb^{3+}–Ho^{3+}, Sm^{3+}–Dy^{3+}, Dy^{3+}–Ho^{3+}, Nd^{3+}–Ho^{3+}, and Er^{3+}–Ho^{3+}.

The second region corresponds to low C_{A-B} but high directional matching in one direction. These pairs are not globally compatible at the manifold level, but the gaps of one ion are well-represented within the gap landscape of the other. This region is topologically consistent with directional sensitizer-like architectures, with $Yb^{3+} \rightarrow Er^{3+}$, $Yb^{3+} \rightarrow Tm^{3+}$ and $Yb^{3+} \rightarrow Nd^{3+}$ as representative examples [2,3,10,11,17,18].

The third region comprises intermediate or mixed pairs, displaying moderate symmetric compatibility and/or incomplete directional asymmetry. These pairs do not show the characteristic joint signature of either limiting architecture and therefore cannot be assigned unambiguously to a broad manifold–manifold or directional sensitizer-like regime.

The fourth region corresponds to low symmetric compatibility and low directional matching in both directions. These pairs show neither broad manifold overlap nor strong directional gap inclusion under the present energy-gap criterion and are therefore described as having a weak topology match.

These four regions are relative interpretive labels within the present LaF_3-based dataset. They do not represent universal numerical classes or direct assignments of experimentally realized energy-transfer mechanisms. The interpretation of an individual pair also considers forward and reverse directional matching, acceptor support coverage and stability under changes in bin width.

The four characteristic regions are summarized in Table 3.

Table 3. Topology-based interpretation of Ln^{3+}–Ln^{3+} coupling architectures.

Mathematical Signature	Topology-Based Interpretation
high C_{A-B}, high $D_{A\rightarrow B}$, high $D_{B\rightarrow A}$	candidate broad manifold–manifold architecture
low C_{A-B}, high $D_{A\rightarrow B}$, low $D_{B\rightarrow A}$	candidate directional sensitizer-like architecture
intermediate C_{A-B} and/or moderate A_D, without either limiting joint signature	intermediate/mixed topology signature
low C_{A-B}, low $D_{A\rightarrow B}$, low $D_{B\rightarrow A}$	weak topology match under the present criterion

The important result is that the lanthanide-pair landscape cannot be represented by a single monotonic scale of overall compatibility. Different co-doped systems may be physically relevant through distinct energetic architectures, as also demonstrated by recent studies of energy-transfer editing, collective transfer networks, Yb^{3+}-mediated migration and spatially organized dopant architectures [2,3,16–21]. A high-C_{A-B} pair and a Yb^{3+}-sensitized pair therefore represent different coupling regimes rather than different positions on a common performance scale. The former reflects broad and reciprocal compatibility between two manifolds, whereas the latter reflects directional gap inclusion from a sparse sensitizer to a richer acceptor.

3.6. Illustrative Multicomponent Absorption Response of the Er^{3+}/Ho^{3+} Sample

The topology map places Er^{3+}–Ho^{3+} in the high-C_{A-B}, low-asymmetry region, corresponding to a candidate manifold–manifold architecture. This pair is also experimentally relevant in lanthanide photonics, particularly in Er^{3+}/Ho^{3+} co-doped systems used for optical thermometry [23]. The assignments of the Er^{3+} and Ho^{3+} absorption bands follow the previous spectroscopic characterization of Er^{3+}/Ho^{3+} co-doped YGG nanogarnets, where the observed absorption bands were attributed to transitions from the Er^{3+} $^4I_{15/2}$ and Ho^{3+} $^5I_8$ ground manifolds to the corresponding excited multiplet levels [23].

In the present work, the absorption spectrum shown in Figure 5 is used as an illustrative material-level example of a multicomponent optical response. The aim is not to repeat a transition-by-transition assignment, extract energy-transfer rates, or test the topology map. Instead, we examined whether the Er^{3+}/Ho^{3+} co-doped spectrum could be described by contributions from both Er^{3+}-only and Ho^{3+}-only reference spectra rather than by a single-ion contribution. The absorption analysis is therefore presented independently of the energy-gap topology calculation.

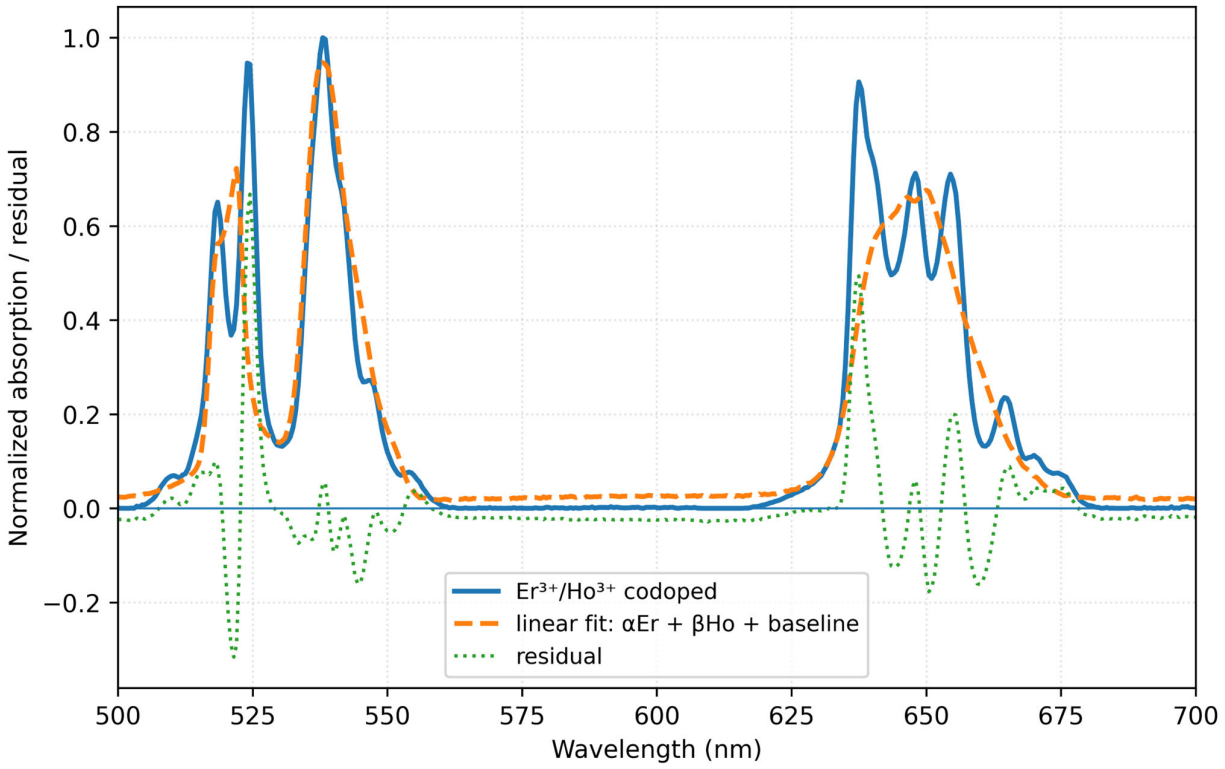


Figure 5. Linear-combination test of the Er^{3+}/Ho^{3+} co-doped absorption spectrum in the shared visible window. The baseline-corrected and normalized Er^{3+}/Ho^{3+} absorption spectrum between 500 and 700 nm is compared with the best linear combination of the Er-only and Ho-only reference spectra, $A_{\mathrm{ErHo}}(\lambda) \approx \alpha A_{\mathrm{Er}}(\lambda) + \beta A_{\mathrm{Ho}}(\lambda) + B(\lambda)$. The fit gives $R^2 = 0.841$, with $\alpha = 0.705$ and $\beta = 0.902$, indicating that the co-doped absorption response in this region is better described by the combined contribution of both Er^{3+} and Ho^{3+} manifolds than by either single-ion contribution alone. The residual highlights the remaining spectral mismatch. This analysis is included as an illustrative multicomponent absorption example and is not used to validate the topology descriptors or to measure $Er^{3+} \leftrightarrow Ho^{3+}$ energy-transfer efficiency.

For this purpose, the baseline-corrected and normalized absorption spectrum of the Er^{3+}/Ho^{3+} co-doped sample was compared with reference spectra obtained from Er-only and Ho-only samples. The co-doped absorption spectrum was fitted using the linear-combination model given by:

$$A_{\mathrm{ErHo}}(\lambda) \approx \alpha A_{\mathrm{Er}}(\lambda) + \beta A_{\mathrm{Ho}}(\lambda) + B(\lambda), \tag{13}$$

where $A_{\mathrm{ErHo}}(\lambda)$ is the absorption spectrum of the co-doped sample, $A_{\mathrm{Er}}(\lambda)$ and $A_{\mathrm{Ho}}(\lambda)$ are the corresponding single-ion reference spectra, α and β are fitted weighting coefficients, and $B(\lambda)$ accounts for a residual baseline contribution. The residual baseline was represented by a first-order term, $\mathrm{B}(\lambda) = \mathrm{c}_0 + \mathrm{c}_1\mathrm{x}(\lambda)$, where $x(\lambda) = \frac{\lambda - (\lambda_{\min}+\lambda_{\max})/2}{\lambda_{\max}-\lambda_{\min}}$ is a centred and normalized wavelength coordinate. The coefficients α, β, c_0, and c_1 were determined simultaneously by least-squares minimization. The three spectra were evaluated on a com-

mon wavelength grid with a spacing of 0.5 nm. The fitted spectra, individual component contributions, residuals, and goodness-of-fit metrics for all tested wavelength intervals are provided in the Supplementary Materials.

The analysis was focused on the 500–700 nm spectral interval. This window contains the most informative shared visible absorption response of the Er^{3+}/Ho^{3+} co-doped sample, including intense and resolved bands associated with the two lanthanide manifolds. It also avoids spectral regions where weak absorption, isolated high-energy features, or baseline contributions dominate the comparison. The same procedure was tested over broader spectral intervals, but the agreement was lower over 300–850 nm and 430–850 nm. The 500–700 nm region therefore provides the most physically focused test of whether the co-doped visible absorption response requires contributions from both ions.

In the 500–700 nm window, the co-doped absorption spectrum was well reproduced by the combined Er-only and Ho-only contributions, with $R^2 = 0.841$. This agreement was substantially better than the corresponding single-ion controls, which gave $R^2 = 0.306$ for an Er-only fit and $R^2 = 0.642$ for a Ho-only fit. Thus, within this spectral interval, the Er^{3+}/Ho^{3+} co-doped response cannot be adequately represented by either single-ion contribution alone. Both manifolds are required to reproduce the main structure of the experimental absorption spectrum.

This result should be interpreted cautiously. Absorption spectra alone do not demonstrate $Er^{3+} \leftrightarrow Ho^{3+}$ energy transfer, since transfer rates, lifetimes, and quantum efficiencies require time-resolved or emission-based measurements [10,11]. The linear-combination analysis was not used to test or validate C_{Er-Ho}. Its role was deliberately limited: it showed that the Er^{3+}/Ho^{3+} co-doped sample exhibited a multicomponent visible absorption response involving both lanthanide ions. No inference about the topology descriptors or about an $Er^{3+} \leftrightarrow Ho^{3+}$ energy-transfer mechanism was drawn from this fit.

A direct experimental validation of the topology assignment would require measurements that probe excited-state dynamics, such as excitation spectra, emission spectra, time-resolved decay curves, concentration-dependent transfer behaviour, and quantum-efficiency measurements. The absorption fit is therefore retained only as an illustrative multicomponent optical response and not as proof of energy transfer.

No new material was synthesized specifically from the topology map in the present work. The submitted Supplementary Materials provide the source energy tables, derived descriptors, bin-width sensitivity analysis, pair-dependent support-coverage controls, and the reproducibility script, allowing the computational part of the framework to be independently reproduced. Prospective validation of the design capability will require selecting candidate ion pairs from different regions of the map, preparing them in selected fluoride and oxide hosts, and comparing the predicted energetic architecture with emission spectra, excitation spectra, lifetime measurements, concentration dependence, and quantum-efficiency analysis.

3.7. Practical Implications for Ln^{3+} Co-Doping Design

The practical value of the present approach lies not in predicting the final optical performance of a material but in providing a pre-spectroscopic map of the energetic architecture of candidate ion pairs.

For pairs located in the manifold–manifold regime, the experimental strategy should account for the possibility of several competing energetic pathways. Such systems may require detailed analysis of cross-relaxation, back-transfer, temperature-dependent redistribution, lifetime changes, and multichannel emission behaviour. A simple one-channel sensitizer–acceptor model may therefore be insufficient [2,3,10,16,19–21].

For pairs located in the directional sensitizer-like regime, the experimental strategy may instead focus on the dominant matching direction. In this case, the relevant physical questions concern sensitizer absorption efficiency, energetic matching with the acceptor, concentration dependence, and the rate of the selected transfer channel [2,3,10,11,17,18].

The transfer direction realized experimentally remains dependent on the host, excitation conditions, and available relaxation pathways. Reverse situations in which Yb^{3+} acts as the acceptor, including $Er^{3+} \rightarrow Yb^{3+}$ and $Pr^{3+} \rightarrow Yb^{3+}$ transfer, have also been reported [24]. This reinforces that the present topology descriptors identify an energetic architecture rather than a unique experimentally realized transfer direction.

A qualitative comparison with experimentally established lanthanide energy-transfer systems supports this interpretation. The $Yb^{3+} \rightarrow Er^{3+}$ and $Yb^{3+} \rightarrow Tm^{3+}$ pairs are classified here as directional sensitizer-like architectures rather than as broad manifold–manifold systems, which is consistent with their widespread use as Yb^{3+}-sensitized upconversion systems. Recent experimental studies further show that Yb^{3+}/Tm^{3+} upconversion can become highly efficient when energy migration, domain size or spatial separation suppresses back-energy-transfer and concentration quenching [20,25]. Conversely, reduced brightness or quenching in otherwise energetically compatible systems can arise from back transfer, concentration-dependent cross-relaxation, surface defects, or high-energy oscillators [25,26]. Thus, the descriptor classification is consistent with the type of coupling architecture observed in established efficient systems, while inefficient behaviour may result from host- and defect-dependent loss channels that the present energy-only descriptors deliberately do not encode.

From the perspective of photon management, the framework could also be extended to architectures in which energy migration, trapping, interfacial transfer, cross-relaxation, and defect-mediated quenching are deliberately engineered rather than treated only as secondary loss channels. In defect-containing hosts, a defect-resolved topology map would require site- or defect-specific spectroscopic data, because vacancies, surface states, hydroxyl-related oscillators, or charge-compensation defects may modify crystal-field splitting, introduce non-radiative loss channels, and redirect energy-migration pathways. Such an extension would move the present ion-pair map toward a material-specific photon-management map, in line with recent work on topology-driven energy-transfer networks and defect passivation in upconversion materials [21,26].

Although the present topology map was constructed from a common LaF_3 spectroscopic reference, oxide-based hosts are also central to rare-earth-doped photonic materials. Recent Er^{3+}/Yb^{3+}-, $Yb^{3+}/Er^{3+}/Ho^{3+}/Tm^{3+}$- and Pr^{3+}/Ho^{3+}-containing oxide, tungstate, and molybdate phosphors illustrate how host composition, dopant concentration, upconversion pathways, back-transfer, thermal quenching, and optical-thermometry requirements determine the final photonic response [27–29]. Compared with fluoride hosts, oxide systems may offer higher chemical and thermal stability, but they can also exhibit different crystal-field strengths, Stark-splitting patterns, site symmetries, phonon energies, and multiphonon relaxation probabilities. Consequently, the descriptor values reported here should not be transferred directly to oxide systems as quantitative host-independent constants. Rather, the same workflow can be applied to oxide-specific Ln^{3+}-level schemes when such data are available, allowing the reference LaF_3 map to be complemented by host-specific energetic maps for phosphors, ceramics, glasses, and crystalline materials.

Recent Sm^{3+}-activated tellurate phosphors further illustrate that lanthanide substitution in oxide-related lattices can modify luminescence chromaticity and thermostability, reinforcing that host chemistry and lattice rigidity affect photonic performance beyond energy-level matching alone [30].

The Er^{3+}/Ho^{3+} absorption example illustrates how multicomponent spectroscopy may be discussed alongside, but independently from, the topology mapping. The linear-combination analysis does not demonstrate energy transfer and is not used to test or validate the calculated topology descriptors. It shows only that the visible absorption response of the co-doped sample contains contributions from both Er^{3+} and Ho^{3+} ions. The absorption result is therefore presented as a material-level spectroscopic example and not as experimental evidence for the candidate manifold–manifold architecture assigned to the Er^{3+}–Ho^{3+} pair by the energy-gap topology map [23].

The topology map therefore does not replace detailed spectroscopic analysis. Rather, it helps identify the type of experimental investigation that is most appropriate for a given energetic architecture. This is the main value of combining C_{A-B} and $D_{A\to B}$: the two descriptors do not simply rank ion pairs but distinguish the type of Ln^{3+}–Ln^{3+} coupling architecture suggested by the underlying 4f manifold topology.

The results establish a distinction that is relevant to lanthanide photonics. Some ion pairs exhibit broad and reciprocal manifold-level compatibility, whereas others exhibit sparse-to-rich directional gap inclusion. Energy-gap topology provides a quantitative screening map for distinguishing these energetic situations before material-specific measurements, host optimization or kinetic modelling are undertaken. It does not determine which mechanism will dominate experimentally, but it indicates which coupling architectures and spectroscopic tests should be prioritized.

3.8. Robustness with Respect to Bin Width and Acceptor Support Coverage

The topology descriptors were recalculated using bin widths of 250, 500, 750, and 1000 cm^{-1} to determine whether the main coupling-architecture distinctions depended on the discretization of the gap-energy axis. Relative to the primary 500 cm^{-1} analysis, the Spearman rank correlation of the complete C_{A-B} landscape was 0.977 for 250 cm^{-1}, 0.989 for 750 cm^{-1} and 0.990 for 1000 cm^{-1}. The corresponding correlations for bidirectional inclusion, D_{bi}, ranged from 0.968 to 0.977, whereas those for directional asymmetry ranged from 0.816 to 0.853. Thus, the absolute descriptor values changed with energetic resolution, but the relative organization of the pairwise landscape remained stable.

The representative manifold–manifold pairs retained high relative compatibility. For Er^{3+}–Ho^{3+}, C_{Er-Ho} varied from 0.764 at 250 cm^{-1} to 0.907 at 1000 cm^{-1} and remained approximately within the upper 10% of all pairwise C_{A-B} values under every binning condition. Its directional matching remained strongly reciprocal, with $D_{Er\to Ho} = 0.992$–1.000 and $D_{Ho\to Er} = 0.714$–0.936. Tb^{3+}–Ho^{3+} and Sm^{3+}–Dy^{3+} similarly remained among the pairs with the highest symmetric compatibility.

The directional character of the Yb^{3+}-containing examples was also preserved. Across the four bin widths, $D_{Yb\to Er}$, $D_{Yb\to Tm}$, and $D_{Yb\to Nd}$ remained equal to 1.000, whereas the reverse values remained low: 0.008–0.050 for $Er^{3+}\to Yb^{3+}$, 0.013 for $Tm^{3+}\to Yb^{3+}$, and 0.013–0.043 for $Nd^{3+}\to Yb^{3+}$. Their directional asymmetries therefore remained between 0.950 and 0.992. At the same time, the support-coverage control showed that complete inclusion of the single Yb^{3+} gap was not equally selective for all acceptors. This result confirms that $D_{Yb\to B} = 1$ should be interpreted as directional inclusion and not as a direct measure of transfer efficiency or resonance uniqueness.

The distinction between broad manifold–manifold compatibility and sparse-to-rich directional inclusion is stable across the tested bin widths. The robustness analysis supports the qualitative architecture map while also showing that absolute descriptor values and the selectivity of one-gap matches must be interpreted with reference to bin width and acceptor support coverage.

4. Conclusions

This work introduced an energy-gap topology framework for comparing lanthanide co-doped systems from the internal energetic structure of their 4f manifolds. By reducing each assigned spectroscopic level scheme to an energy-only manifold and calculating all internal energy separations, each Ln^{3+} ion was represented by a gap-density distribution $P_{Ln}(\Delta E)$. This representation provides a transition-label-independent description of the energetic separations available within each ion.

The main result is that a single compatibility descriptor is insufficient to describe the different energetic situations encountered in lanthanide co-doping. The symmetric descriptor C_{A-B} measures global similarity between complete gap distributions and identifies pairs with broad manifold-level compatibility. The directional descriptor $D_{A\to B}$ measures the inclusion of the gaps of one ion within the occupied support of another and reveals strongly asymmetric sparse-to-rich matching that is not captured by C_{A-B} alone.

The central methodological advance is not the reassignment of Ln^{3+} energy levels or the proposal of a new microscopic transfer mechanism. Instead, it is the introduction of a whole-manifold framework that replaces transition-by-transition matching with a comparison of complete internal gap distributions. By distinguishing global reciprocal compatibility from directional gap inclusion, the framework shows that manifold–manifold and sparse sensitizer–acceptor pairs represent different energetic coupling architectures rather than different positions on a single compatibility scale.

The combined use of the two descriptors separates characteristic regions of the pairwise landscape. Pairs such as Tb^{3+}–Ho^{3+}, Sm^{3+}–Dy^{3+}, Dy^{3+}–Ho^{3+}, Nd^{3+}–Ho^{3+}, and Er^{3+}–Ho^{3+} exhibit high symmetric compatibility and reciprocal directional inclusion, consistent with candidate manifold–manifold architectures. In contrast, the Yb^{3+}-containing examples exhibit low global manifold compatibility, complete forward inclusion of the single Yb^{3+} gap and very low reverse inclusion, producing a strongly directional topology signature.

For sparse one-gap ions, $D_{A\to B} = 1$ must be interpreted cautiously. It indicates that the donor gap lies within the occupied support of the acceptor manifold; it does not demonstrate transfer efficiency, unique resonance, or statistical significance. The support-coverage control showed that identical directional inclusion values may occur within acceptor manifolds having substantially different fractional coverage. Directional matching must therefore be interpreted jointly with C_{A-B}, reverse inclusion, asymmetry, and acceptor support coverage.

The principal architecture distinctions were stable with respect to the gap-distribution bin width. Recalculation using 250, 500, 750, and 1000 cm^{-1} bins preserved the relative organization of the pairwise compatibility landscape, with Spearman correlations of 0.977–0.990 for C_{A-B} relative to the primary 500 cm^{-1} analysis. Representative manifold–manifold and directional Yb^{3+}-containing pairs retained their contrasting topology signatures across all tested resolutions.

The Er^{3+}/Ho^{3+} absorption analysis provides an illustrative material-level example in which both ionic manifolds contribute to the measured optical response. It is not used as a validation of the calculated topology descriptors or of an $Er^{3+} \leftrightarrow Ho^{3+}$ energy-transfer mechanism. The co-doped visible absorption spectrum was better reproduced by the combined Er-only and Ho-only contributions than by either single-ion contribution alone. This result demonstrates a multicomponent absorption response involving both lanthanide manifolds, but it does not constitute a measurement or direct validation of $Er^{3+} \leftrightarrow Ho^{3+}$ energy-transfer efficiency.

The calculated values are based on multiplet-centre energies reported for a common LaF_3 reference. They should therefore not be treated as universal constants for all host materials. Crystal-field shifts, Stark structures, site symmetries, phonon energies, dopant

concentrations, and ion–ion spatial organization remain essential in determining the experimentally realized transfer pathways and final optical performance.

Consequently, the framework should be regarded as a first screening layer to be combined with host-specific level data and, where possible, physically weighted descriptors. Extensions based on oxide-specific datasets, Stark-resolved manifolds, or transition-strength weighting would allow the same mapping concept to be tested against experimentally efficient and inefficient Ln^{3+} energy-transfer systems.

Future work should therefore use the present map prospectively by selecting ion pairs from different topology regions and testing them in host-specific experimental systems. A direct validation of the design capability would require synthesis and spectroscopic comparison of selected fluoride and oxide materials, including emission and excitation spectra, lifetime analysis, concentration-dependent studies, and quantum-efficiency measurements.

A complementary direction would be to combine energy-gap topology with photon-management and defect-resolved descriptions, so that engineered migration networks, traps, and quenching centres can be incorporated into host-specific versions of the map.

Consequently, energy-gap topology does not predict whether a co-doped material will display strong emission or efficient energy transfer. Its value lies in providing a reproducible pre-spectroscopic screening map of the energetic architecture suggested by a pair of Ln^{3+} manifolds. By distinguishing broad reciprocal compatibility from sparse-to-rich directional inclusion, the framework can guide the selection of candidate ion pairs and the design of subsequent host-specific, kinetic, and time-resolved spectroscopic investigations.

Supplementary Materials: The following supporting information can be downloaded at: https://www.mdpi.com/article/10.3390/photonics13080733/s1, Table S1: Verified multiplet-centre energies of the Ln^{3+} ions used in the analysis. Term labels, J values, source document, source location, data type and notes are retained for traceability; only ion identity and energy coordinates entered the topology calculations, while 4f occupancy was retained for ordering and annotation [7,22]; Table S2: Complete pairwise topology descriptors calculated at the primary bin width of 500 cm^{-1}. C_{A-B} is the symmetric compatibility descriptor, $D_{A\to B}$ and $D_{B\to A}$ are directional gap-inclusion values, D_{bi} is the lower directional value, A_D is the directional asymmetry, and $F_A^{(A,B)}$ and $F_B^{(A,B)}$ are pair-dependent support coverages; Table S3: Bin-width sensitivity analysis for all Ln^{3+} pairs. The full calculation was repeated using bin widths of 250, 500, 750 and 1000 cm^{-1}; rank-correlation summaries and representative pair results are included; Table S4: Ordered-pair support-coverage controls at 500 cm^{-1}. $F_B^{(A,B)}$ gives the fraction of bins occupied by acceptor B within the active pairwise energy domain $[0, \max(\max G_A, \max G_B)]$; Figure S1: Sensitivity of the symmetric compatibility descriptor C_{A-B} to gap-distribution bin width for representative manifold–manifold and Yb^{3+}-containing pairs; Figure S2: Sensitivity of the directional asymmetry A_D to gap-distribution bin width for representative manifold–manifold and Yb^{3+}-containing pairs; Figure S3: Pair-dependent acceptor support coverage for the $Yb^{3+} \to Er^{3+}$, $Yb^{3+} \to Tm^{3+}$ and $Yb^{3+} \to Nd^{3+}$ examples at the primary bin width of 500 cm^{-1}. Identical $D_{\mathrm{Yb}\to B} = 1$ values occur within acceptor supports of different fractional breadth; Machine-Readable Data: Machine-readable exports of Tables S1–S4, descriptor matrices, and numerical data underlying manuscript Figures 2–5 and Supplementary Figures S1–S3; Reproducibility: Python script used to recalculate the energy-gap distributions, pairwise descriptors, bin-width sensitivity, and pair-dependent support-coverage controls; Source Data: Verified LaF_3 energy-level tables and absorption spectra used in the illustrative Er^{3+}/Ho^{3+} analysis.

Author Contributions: Conceptualization, H.C.V.; methodology, H.C.V.; software, M.G.M.; validation, H.C.V. and M.G.M.; formal analysis, H.C.V.; investigation, H.C.V.; resources, H.C.V.; data curation, M.G.M.; writing—original draft preparation, H.C.V.; writing—review and editing, H.C.V. and M.G.M.; visualization, H.C.V. and M.G.M.; supervision, H.C.V.; project administration, H.C.V. All authors have read and agreed to the published version of the manuscript.

Funding: This research received no external funding.

Data Availability Statement: The data and analysis code supporting the findings of this study are available in the Supplementary Materials.

Conflicts of Interest: The authors declare no conflicts of interest.

References

1. Bünzli, J.-C.G. On the design of highly luminescent lanthanide complexes. *Coord. Chem. Rev.* **2015**, *293–294*, 19–47. [CrossRef]
2. Qin, X.; Xu, J.; Wu, Y.; Liu, X. Energy-transfer editing in lanthanide-activated upconversion nanocrystals: A toolbox for emerging applications. *ACS Cent. Sci.* **2019**, *5*, 29–42. [CrossRef] [PubMed]
3. Cheng, X.; Tu, D.; Zheng, W.; Chen, X. Energy transfer designing in lanthanide-doped upconversion nanoparticles. *Chem. Commun.* **2020**, *56*, 15118–15132. [CrossRef] [PubMed]
4. Dieke, G.H. *Spectra and Energy Levels of Rare Earth Ions in Crystals*; Crosswhite, H.M., Crosswhite, H., Eds.; Interscience Publishers: New York, NY, USA, 1968.
5. Peijzel, P.S.; Meijerink, A.; Wegh, R.T.; Reid, M.F.; Burdick, G.W. A complete $4f^n$ energy level diagram for all trivalent lanthanide ions. *J. Solid State Chem.* **2005**, *178*, 448–453. [CrossRef]
6. Wybourne, B.G. *Spectroscopic Properties of Rare Earths*; Interscience Publishers: New York, NY, USA, 1965.
7. Carnall, W.T.; Goodman, G.L.; Rajnak, K.; Rana, R.S. A systematic analysis of the spectra of the lanthanides doped into single crystal LaF_3. *J. Chem. Phys.* **1989**, *90*, 3443–3457. [CrossRef]
8. Förster, T. Zwischenmolekulare Energiewanderung und Fluoreszenz. *Ann. Phys.* **1948**, *437*, 55–75. [CrossRef]
9. Dexter, D.L. A theory of sensitized luminescence in solids. *J. Chem. Phys.* **1953**, *21*, 836–850. [CrossRef]
10. Auzel, F. Upconversion and anti-Stokes processes with f and d ions in solids. *Chem. Rev.* **2004**, *104*, 139–174. [CrossRef] [PubMed]
11. Lahoz, F.; Pérez-Rodríguez, C.; Halder, A.; Das, S.; Paul, M.C.; Pal, M.; Bhadra, S.K.; Vasconcelos, H.C. Complete energy transfer due to rare-earth phase segregation in optical fiber preform glasses. *J. Appl. Phys.* **2011**, *110*, 083121. [CrossRef]
12. Judd, B.R. Optical absorption intensities of rare-earth ions. *Phys. Rev.* **1962**, *127*, 750–761. [CrossRef]
13. Ofelt, G.S. Intensities of crystal spectra of rare-earth ions. *J. Chem. Phys.* **1962**, *37*, 511–520. [CrossRef]
14. Riseberg, L.A.; Moos, H.W. Multiphonon orbit-lattice relaxation of excited states of rare-earth ions in crystals. *Phys. Rev.* **1968**, *174*, 429–438. [CrossRef]
15. Weber, M.J. Luminescence decay by energy migration and transfer: Observation of diffusion-limited relaxation. *Phys. Rev. B* **1971**, *4*, 2932–2939. [CrossRef]
16. Teitelboim, A.; Tian, B.; Garfield, D.J.; Fernandez-Bravo, A.; Gotlin, A.C.; Schuck, P.J.; Cohen, B.E.; Chan, E.M. Energy transfer networks within upconverting nanoparticles are complex systems with collective, robust, and history-dependent dynamics. *J. Phys. Chem. C* **2019**, *123*, 2678–2689. [CrossRef]
17. Zhou, B.; Yan, L.; Huang, J.; Liu, X.; Tao, L.; Zhang, Q. NIR II-responsive photon upconversion through energy migration in an ytterbium sublattice. *Nat. Photonics* **2020**, *14*, 760–766. [CrossRef]
18. Mei, S.; Zhou, J.; Sun, H.-T.; Cai, Y.; Sun, L.-D.; Jin, D.; Yan, C.-H. Networking state of ytterbium ions probing the origin of luminescence quenching and activation in nanocrystals. *Adv. Sci.* **2021**, *8*, 2003325. [CrossRef] [PubMed]
19. Zhang, Y.; Wen, R.; Hu, J.; Guan, D.; Qiu, X.; Zhang, Y.; Kohane, D.S.; Liu, Q. Enhancement of single upconversion nanoparticle imaging by topologically segregated core-shell structure with inward energy migration. *Nat. Commun.* **2022**, *13*, 5927. [CrossRef] [PubMed]
20. Li, F.; Tu, L.; Zhang, Y.; Huang, D.; Liu, X.; Zhang, X.; Du, J.; Fan, R.; Yang, C.; Krämer, K.W.; et al. Size-dependent lanthanide energy transfer amplifies upconversion luminescence quantum yields. *Nat. Photonics* **2024**, *18*, 440–449. [CrossRef]
21. Gu, W.; Lamon, S.; Yu, H.; Zhang, Q.; Gu, M. Topology-driven energy transfer networks for upconversion stimulated emission depletion microscopy. *Light Sci. Appl.* **2025**, *14*, 395. [CrossRef] [PubMed]
22. Carnall, W.T.; Crosswhite, H.; Crosswhite, H.M. *Energy Level Structure and Transition Probabilities in the Spectra of the Trivalent Lanthanides in LaF_3*; Report No. ANL-78-XX-95; Argonne National Laboratory: Argonne, IL, USA, 1978. [CrossRef]
23. Soler-Carracedo, K.; Martín, I.R.; Lahoz, F.; Vasconcelos, H.C.; Lozano-Gorrín, A.D.; Martín, L.L.; Paz-Buclatin, F. Er^{3+}/Ho^{3+} codoped nanogarnet as an optical FIR based thermometer for a wide range of high and low temperatures. *J. Alloys Compd.* **2020**, *847*, 156541. [CrossRef]
24. Kaczmarek, A.M.; Kaczmarek, M.K.; Van Deun, R. Er^{3+}-to-Yb^{3+} and Pr^{3+}-to-Yb^{3+} energy transfer for highly efficient near-infrared cryogenic optical temperature sensing. *Nanoscale* **2019**, *11*, 833–837. [CrossRef] [PubMed]
25. Huang, D.; Li, F.; Ågren, H.; Chen, G. Inhibiting concentration quenching in Yb^{3+}-Tm^{3+} upconversion nanoparticles by suppressing back energy transfer. *Nat. Commun.* **2025**, *16*, 4218. [CrossRef] [PubMed]
26. Suo, H.; Zhao, P.; Zhang, X.; Guo, Y.; Guo, D.; Chang, J.; Chen, J.; Li, P.; Wang, Z.; Wei, H.; et al. Bright upconversion over extended temperatures enabled by an organic surface layer. *Nat. Commun.* **2025**, *16*, 3249. [CrossRef] [PubMed]

27. Li, Q.; Zhang, Z.; Liu, J.; Huang, Z.; Li, K. Delayed concentration quenching and multi-dimensional color tunability in Er^{3+}/Yb^{3+}-doped $NaGdSnWO_7$ phosphors enabling optical anti-counterfeiting and information encryption, latent fingerprint detection, and temperature sensing. *Mater. Today Chem.* **2026**, *55*, 103847. [CrossRef]
28. Li, Q.; Zhang, Z.; Li, K. Tailoring up-conversion luminescence and enhancing temperature sensitivity through Tm^{3+} co-doping in Yb^{3+}, Er^{3+}/Ho^{3+} activated Ca(Gd,La)$SbWO_8$ phosphors. *Ceram. Int.* **2026**, *52*, 7655–7666. [CrossRef]
29. Zhou, C.; Liu, J.; Lv, J.; Chen, Y.; Li, K. Luminescence and temperature sensing properties of novel Pr^{3+}, Ho^{3+} co-doped $KBaGd(Mo/WO_4)_3$ phosphors. *Mater. Res. Bull.* **2026**, *201*, 114151. [CrossRef]
30. Wang, R.; Xie, J.; Haider, A.A.; Zhang, H.; Li, Y.; Li, Z.; Xu, Y.; Jiang, M.; Zhang, J.; Qian, W.; et al. Remarkable role of lanthanide substitution on luminescence chromaticity and thermostability of Sm^{3+}-activated tellurate phosphors synthesized via microwave-assisted method. *J. Alloys Compd.* **2025**, *1026*, 180511. [CrossRef]

Disclaimer/Publisher's Note: The statements, opinions and data contained in all publications are solely those of the individual author(s) and contributor(s) and not of MDPI and/or the editor(s). MDPI and/or the editor(s) disclaim responsibility for any injury to people or property resulting from any ideas, methods, instructions or products referred to in the content.